Heliyon 10 (2024) e35236

Contents lists available at ScienceDirect

Heliyon

journal homepage: www.cell.com/heliyon

Research article

Automated classification of angle-closure mechanisms based on anterior segment optical coherence tomography images via deep learning

Ye Zhang [a,1], Xiaoyue Zhang [b,1], Qing Zhang [c], Bin Lv [b], Man Hu [d], Chuanfeng Lv [b], Yuan Ni [b], Guotong Xie [b,e,f,**], Shuning Li [a,***], Nazlee Zebardast [g], Yusrah Shweikh [g,h], Ningli Wang [a,c,*]

[a] *Beijing Tongren Eye Center, Beijing Key Laboratory of Ophthalmology & Visual Science, Beijing Tongren Hospital, Capital Medical University, Beijing, China*
[b] *Ping an Healthcare Technology, Beijing, China*
[c] *Beijing Institute of Ophthalmology, Beijing, China*
[d] *National Key Discipline of Pediatrics, Ministry of Education, Department of Ophthalmology, Beijing Children's Hospital, Capital Medical University, China*
[e] *Ping an Health Cloud Company Limited, Shenzhen, China*
[f] *Ping an International Smart City Technology Company Limited, Shenzhen, China*
[g] *Massachusetts Eye and Ear Infirmary, Harvard Medical School Department of Ophthalmology, Boston, MA, USA*
[h] *Sussex Eye Hospital, University Hospitals Sussex NHS Foundation Trust, Sussex, UK*

ARTICLE INFO

Keywords:
Deep learning
Angle-closure mechanisms
Anterior segment optical coherence tomography
Automated classification

ABSTRACT

Purpose: To develop and validate deep learning algorithms that can identify and classify angle-closure (AC) mechanisms using anterior segment optical coherence tomography (AS-OCT) images.

Methods: This cross-sectional study included participants of the Handan Eye Study aged ≥35 years with AC detected via gonioscopy or on the AS-OCT images. These images were classified by human experts into the following to indicate the predominant AC mechanism (ground truth): pupillary block, plateau iris configuration, or thick peripheral iris roll. A deep learning architecture, known as comprehensive mechanism decision net (CMD-Net), was developed to simulate the identification of image-level AC mechanisms by human experts. Cross-validation was performed to optimize and evaluate the model. Human-machine comparisons were conducted using a held-out and separate test sets to establish generalizability.

Results: In total, 11,035 AS-OCT images of 1455 participants (2833 eyes) were included. Among these, 8828 and 2.207 images were included in the cross-validation and held-out test sets, respectively. A separate test was formed comprising 228 images of 35 consecutive patients with

* Corresponding author. Beijing Institute of Ophthalmology, Beijing Tongren Eye Center, Beijing Tongren Hospital, Capital Medical University; Beijing Key Laboratory of Ophthalmology and Visual Sciences. No. 1 Dong Jiao Min Xiang Street, Dongcheng District, Beijing, 100730, China.
** Corresponding author. Ping An Healthcare Technology, Beijing, China, 100027; Ping An Health Cloud Company Limited, Shenzhen, China, 518000; Ping An International Smart City Technology Company Limited, Shenzhen, 518000, China.
*** Corresponding author. Beijing Tongren Eye Center, Beijing Tongren Hospital, Capital Medical University; Beijing Key Laboratory of Ophthalmology and Visual Sciences. No. 1 Dong Jiao Min Xiang Street, Dongcheng District, Beijing, 100730, China.
E-mail addresses: xieguotong@pingan.com.cn (G. Xie), lishuningqd@163.com (S. Li), wningli@vip.163.com (N. Wang).
[1] These two authors contributed equally to this work and should be considered as co-first authors.

https://doi.org/10.1016/j.heliyon.2024.e35236
Received 18 February 2024; Received in revised form 24 July 2024; Accepted 25 July 2024
Available online 26 July 2024

AC detected via gonioscopy at our eye center. In the classification of AC mechanisms, CMD-Net achieved a mean area under the receiver operating characteristic curve (AUC) of 0.980, 0.977, and 0.988 in the cross-validation, held-out, and separate test sets, respectively. The best-performing ophthalmologist achieved an AUC of 0.903 and 0.891 in the held-out and separate test sets, respectively. And CMD-Net outperformed glaucoma specialists, achieving an accuracy of 89.9 % and 93.0 % compared to 87.0 % and 86.8 % for the best-performing ophthalmologist in the held-out and separate test sets, respectively.

Conclusions: Our study suggests that CMD-Net has the potential to classify AC mechanisms using AS-OCT images, though further validation is needed.

1. Introduction

Nearly half of all cases of glaucoma-related blindness can be attributed to primary angle-closure glaucoma (PACG), which affects 21 million individuals worldwide [1,2]. China, where approximately 3.1 million individuals are blind in at least one eye and 1.6 million individuals are blind in both eyes secondary to angle-closure (AC) disease, accounts for 48 % of PACG cases globally [1–3].

A universal classification has not been established for AC; however, the classification system proposed by the International Society of Geographic and Epidemiologic Ophthalmology has become the most frequently cited and used system [4]. The term primary angle-closure disease (PACD) encompasses primary angle-closure suspects (PACS), primary angle-closure (PAC), PACG, and acute angle-closure crisis (AACC) [4].

The subtypes of PACD have varying underlying AC mechanisms [5]. Pupillary block (PB) is the major underlying mechanism of AACC [5–8]. Chronic AC may occur in PACS, PAC, and PACG due to a variable combination of iris-angle crowding mechanisms in addition to PB, including plateau iris configuration (PIC), relatively anterior iris insertion, thick peripheral iris roll (TPIR), or exaggerated lens vault (ELV) [6,8–10]. Multiple mechanisms of AC act in tandem in the majority of cases of chronic PACD [9,11].

Discerning the underlying mechanisms of PACD in individual cases is necessary and has important implications in the selection of optimal treatment [6,7,10,12–16]. Gonioscopy, a challenging clinical technique with limited interobserver agreement, is the most frequently used method for the assessment of AC [17]. Accurate, automated methods that can identify AC mechanisms will assist in the diagnosis and treatment decision-making. In addition, such methods will help mitigate the risk of misdiagnosing PB as the dominant mechanism and consequent overuse of laser peripheral iridotomy (LPI) for prophylaxis and treatment, which will also benefit resource allocation.

Anterior segment optical coherence tomography (AS-OCT) plays an important role in the care of patients with PACD. Its excellent repeatability and reproducibility have enabled non-contact quantitative and qualitative analyses of anterior segment parameters [12,18]. Moreover, AS-OCT can acquire images of each of the four anterior chamber quadrants and a circumferential scan simultaneously [18,19].

Previous studies have established methods for classifying AC mechanisms using AS-OCT images, which rely on the input of clinicians or researchers [11,20,21]. A previous study reported a good intra-observer correlation between the identification of AC mechanisms using ultrasound biomicroscopy (UBM) versus AS-OCT images (kappa = 0.87) [22]. Nevertheless, automation is an attractive progression as it circumvents the limitations associated with manual methods, such as subjectivity and clinician time constraints.

There is a significant precedent for the use of deep learning approaches in ophthalmology, which has been enabled by the convergence of advanced computational techniques and the availability of large datasets [23–25]. However, the application of deep learning approaches to the qualitative assessment of AC mechanisms remains limited. Challenges related to its implementation include the acquisition of large sets of AS-OCT images and complex feature recognition that require a comprehensive long-range and detail-oriented judgment which most convolutional neural networks (CNNs) are incapable of. Moreover, identifying the dominant AC mechanism in the presence of minor mechanisms remains challenging.

This study aimed to establish a large sample size of AS-OCT images for the exploration of AC mechanisms to enable the development of deep learning algorithms. In addition, a deep learning system, known as comprehensive mechanism decision net (CMD-Net), was developed based on a state-of-the-art hierarchical vision transformer architecture that used the "distilling strategy" to incorporate attention mechanisms to enable whole-image differentiation of specific tissue features [26].

2. Methods

2.1. Participants and ophthalmic examination

The participants of this study were selected from the 5-year follow-up cohort of the Handan Eye Study (HES), a population-based study. The HES enrolled adults aged ≥30 years residing in rural areas in Handan County, Hebei Province, China [27]. Surviving members of the original HES cohort were re-examined for the 5-year follow-up between May 2012 and June 2013 [28].

All participants underwent a comprehensive ophthalmic examination, including visual acuity measurement using the participant's refractive correction, best-corrected visual acuity measurement, objective and subjective refraction, slit-lamp biomicroscopy, AS-OCT imaging, visual field testing, applanation tonometry, A-scan ultrasound biometry, and fundus examination. One in ten participants, in

addition to all participants with a limbal anterior chamber depth ≤40 % according to the modified van Herick system, an intraocular pressure (IOP) > 21 mmHg, and those with a history of glaucoma or suspected glaucoma underwent gonioscopy. Gonioscopy was performed by glaucoma specialists using a one-mirror Goldmann gonioscopic lens (Ocular Instruments, Bellevue, WA) at × 25 magnification under no ambient illumination at baseline and follow-up.

Participants aged ≥35 years at the time of the follow-up who were diagnosed with AC via gonioscopy or on AS-OCT (defined as contact between the iris and any part of the angle wall anterior to the scleral spur for ≥2 quadrants) at baseline or follow-up were included in this analysis [29]. AC was detected via gonioscopy was defined as the presence of PACS (iridotrabecular contact ≥180° on static gonioscopic examination, IOP ≤21 mmHg, no peripheral anterior synechiae [PAS], and healthy optic nerves), PAC (IOP >21 mmHg or the presence of PAS), or PACG (PAC with glaucomatous optic neuropathy [GON]).

Participants meeting any of the following criteria were excluded from the analysis:

- History of intraocular surgery, penetrating eye injury, or corneal disorders causing opacity or edema precluding anterior chamber assessment.
- Receiving topical and/or systemic medications that could modulate the iris or angle configuration (cholinergics or anticholinergics; adrenergic agonists or antagonists; serotonin; norepinephrine; and dopaminergic drugs, including their precursors and dopamine reuptake inhibitors, monoamine oxidase inhibitors, opioid agonists and antagonists, and histamine receptor antagonists).
- History of AACC, previous LPI, or argon laser peripheral iridoplasty (ALPI) with potential alterations in the AC mechanisms or consecutive iris atrophy and sphincter action loss.

The study was approved by the Ethics Committee of Beijing Tongren Hospital and performed in accordance with the tenets of the Declaration of Helsinki. All participants provided verbal and written informed consent.

2.2. AS-OCT image acquisition

AS-OCT image acquisition was performed using a ZEISS Visante™ ASOCT Model 1000 device (Carl Zeiss Meditec, Inc., Dublin, CA, USA) under standardized dim illumination (approximately 3 lx). An internal fixation target was presented with the participants' refractive correction in place to acquire measurements in an unaccommodated state. All acquisitions were obtained by a trained ophthalmic technician blinded to the participants' examination data. All images were acquired in the "anterior segment quadrant" mode at the 0°–180°, 45°–225°, 90°–270°, and 135°–315° meridians with the images centered on the pupil. The eyelids were retracted gently to improve vertical image acquisition while avoiding inadvertent pressure on the globe. Image acquisition was repeated if the visibility of the scleral spur was poor.

2.3. Ground truth labeling

An ophthalmologist trained in image examination labeled each AS-OCT image as PB, PIC, TPIR, or ELV via visual inspection to denote the major AC mechanism. Image labeling was later adjudicated by a fellowship-trained ophthalmologist specializing in glaucoma. The labelers had access to the unlabeled images only and were blinded to the participants' data. A senior glaucoma specialist was consulted for final arbitration in the case of disagreements.

The AC mechanisms were categorized as follows:

(1) PB (Supplementary Fig. 1A): Convex iris profile with a minimal zone of iris-lens contact present centrally and a shallow peripheral anterior chamber.
(2) PIC (Supplementary Fig. 1B): The peripheral iris rises from its root in apposition or close proximity to the angle wall, then turns sharply away from the angle toward the visual axis. The central anterior chamber is relatively deep, with a shallow periphery.
(3) TPIR (Supplementary Fig. 1C): A thick iris forms prominent peripheral circumferential folds that occupy a large proportion of the angle. The central anterior chamber is relatively deep, whereas the periphery is shallow.
(4) ELV (Supplementary Fig. 1D): Eyes with a shallow central anterior chamber in which the iris appears to drape over the anterior surface of the lens, resulting in a "volcano-like" or "Vesuvian" profile. The space between the surface of the iris and the endothelium is markedly decreased without any increase in the curvature of the iris [9,20,21].

Images wherein the major AC mechanism was labeled as ELV were excluded from the analysis as they were relatively few in number (n = 198). Thus, the ground truth labeling comprised PB, PIC, and TPIR labels. Before labeling the images used for the analyses, the graders were requested to label a dataset comprising the same 200 images to test the intra-observer agreement. A Kappa value of 0.75 was achieved.

2.4. Image preprocessing and data augmentation

The central 757 × 375 pixels of each AS-OCT image, which contained the entire anterior chamber, were selected and cropped as the region of interest (ROI). By focusing on this central region, we excluded peripheral areas that do not contain relevant clinical information, reducing noise and simplifying computational demands. After extracting the ROI, the images were reshaped into a dimension of 224 × 224 pixels. This uniform size is not only computationally efficient but also matches the typical input size for the pre-trained

models. Then images were normalized into the same range of intensity, typically adjusted the pixel values to have approximately zero mean and unit variance, which accelerates the convergence during model training.

Before fed into the model, data augmentation was conducted for a better generalization, enhancing the model's ability to generalize across various clinical scenarios. The image diversity was enriched by random rotation between -20° and 20°, mimicking the potential tilting of patients' eyes during scans; and random shift up to 10 pixels in both horizontal and vertical directions, simulating slight misalignments caused by patient movements; scaling transformations adjusting natural size variations among different individuals or different imaging settings; and random horizontal flipping that doubles the effective dataset size regarding left-right variations of anatomical structures.

2.5. Algorithm design

We designed a deep learning model called CMD-Net for classifying AC mechanisms based on AS-OCT images. CMD-Net combines the advantages of two powerful architectures: vision transformers and distilling strategies.

The algorithm employs a teacher-student strategy known as distilling, where a CNN serves as the "teacher" model and a vision transformer acts as the "student" model.

Labels were assigned to the major AC mechanism only during ground truth labeling, despite the likelihood of each image depicting coexisting minor mechanisms. It was deemed preferable for the model to learn the relationships between all contributory AC mechanisms to improve its performance and minimize labeling noise, which may arise if the sole focus is on the major mechanism. Hence, distilling was incorporated to establish an implication relationship between the image and minor AC mechanisms.

The output probability of the specific class of a deep learning model is typically produced by a softmax activation function that converts the logit computed for each class into a probability by comparison with other logits.

$$q_i = \frac{\exp\left(z_i/T\right)}{\sum_j \exp\left(z_i/T\right)}$$

where the parameter "temperature" (T) is normally set to one in the distilling theory [30]. However, a high temperature value could be advantageous in our task as it would soften the probability distribution over the three classes, which could smoothen and reduce the noise associated with the hard labels by enabling smaller possibilities to branch from the main mechanism.

A convolutional network paradigm, Inception-V4, was trained as a teacher model in a previous experiment [31]. The output logits were processed through a distillation module with the temperature value set to 100, and soft labels were produced for the student model.

A Swin-transformer model was developed as the student model to automatically classify AC mechanisms in a manner that mimics that of ophthalmologists. By leveraging attention mechanisms, the transformer architecture can capture long-term dependencies to identify the relationships among specific tissue features over whole images for different mechanisms. A minuscule but efficient version of the Swin-transformer, the Swin-T, was selected as the classification backbone. Unlike CNN operations, the grayscale AS-OCT images passed through a splitting module when input into Swin-T and were divided into non-overlapping patches before entering the main architecture.

The main architecture contained four types of stages, each incorporating a linear embedding or patch merging module and Swin-transformer blocks to jointly produce a hierarchical representation. In contrast to typical transformers, Swin replaces the multi-head self-attention module by shifting the window-based self-attention module and building connections among windows in the preceding layers to achieve efficient batch computation [26]. Let Q be the query, K the key and V the value matrix, self-attention similarity is calculated as the following formula, where d denotes the query/key dimension and B stands for the positioning bias [26].

$$Attention(Q, K, V) = SoftMax\left(\frac{QK^T}{\sqrt{d}} + B\right)V$$

For the Swin Transformer, the architecture is organized into four stages with block numbers set as 2, 2, 6, and 2, respectively. The model undergoes a comprehensive pre-training phase on the ImageNet-22K dataset, which comprises approximately 14.2 million images spanning 22,000 classes. This extensive pre-training helps in developing robust feature representations that can generalize well across a wide range of tasks and datasets. Additionally, the training process includes a warm-up period, during which learning rates are gradually increased. This warm-up phase is crucial for stabilizing the training dynamics early in the training process, which helps in achieving better convergence and overall performance.

The deep learning system was implemented using PyTorch. The models were pre-trained on the ImageNet dataset and trained with a batch size of 256 using the Adam optimizer [32]. All experiments were conducted on a server with 32 central processing units, using four NVIDIA Tesla P100 graphic processing units.

All AS-OCT images were randomly divided into five independent datasets. Among them, 80 % were used to form the cross-validation set for four-fold cross-validation (for the training and validation phases). A held-out test was conducted with the remaining 20 % (held-out test set) to evaluate the final performance of the artificial intelligence (AI) model against ophthalmologists. The training and test sets comprised images split at the image level and were not categorized by eye or patient type. In addition, a separate dataset (separate test set) comprising 228 AS-OCT images of 35 participants with PACD (clinic-based samples) aged $\geq$40 years from our eye center was also used to test generalizability. This dataset was collected independently of those used for the training, validation, and testing phases.

2.6. Evaluation and interpretation

Participant characteristics are presented as mean ± standard deviation (SD) for continuous data and as frequency (%) for categorical variables.

Cross-validation and human-machine comparisons were conducted to evaluate the performance of the model and access the generalizability. To investigate the contributions of the distilling strategy, we conducted experiments on the cross-validation set using CMD-Net and a baseline model lacking a distilling module (Swin-Transformer). For human-machine comparison, three senior ophthalmologists specializing in glaucoma, that had 5–10 years of clinical experience, were independent from those who were involved in ground truth labeling, and were blinded to patient data, classified the AC mechanisms using the AS-OCT images.

The area under the receiver operating characteristic (ROC) curve (AUC) with 95 % confidence intervals (CI), accuracy, sensitivity, specificity, F1 score, positive predictive value (PPV), and negative predictive value (NPV) were calculated to evaluate the performance of CMD-Net [33]. The ROC curve is typically used for binary classification measurements; however, it can be used for multi-class classification measurements by converting predictions into several one-versus-the-rest binary classifications [34]. The ROC curve can then be plotted from these binary classifications using the micro-averaging technique [34]. Raw and normalized confusion matrices were applied to visualize specific performance with a table layout in which each row represented the true class and each column represented the predicted class to intuitively demonstrate the distribution of mislabeled instances via a color overlay.

A gradient-weighted class activation mapping (grad-CAM) technique, which has been used in several AI clinical applications to visualize the regions leading to final predictions, was used to create heat maps for interpretation [35]. This study applied this visualization method to both CMD-Net and Inception-V4, which served as the teacher model, to provide insight into the differences

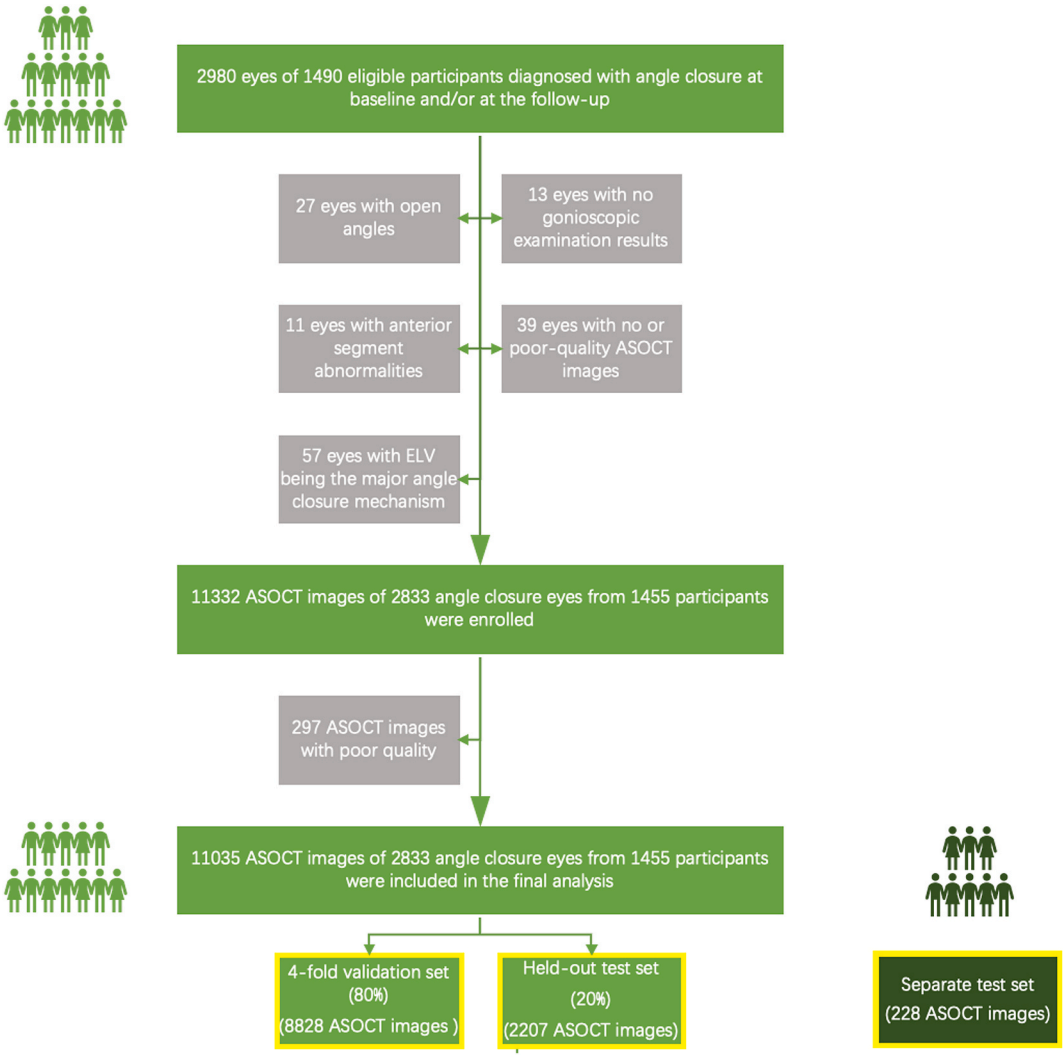

Fig. 1. Flow chart showing the enrolment of participants, eyes, and ASOCT images. AS-OCT: anterior segment optical coherence tomography; ELV: exaggerated lens vault.

between CMD-Net and the state-of-the-art CNN-based method.

3. Results

3.1. Key findings

Our deep learning model (CMD-Net) accurately classified AC mechanisms from AS-OCT images and outperformed both human experts and baseline models. The model showed good generalizability when tested on an independent dataset. Moreover, CMD-Net focused on clinically relevant eye structures when making decisions, similar to how experts examine images.

3.2. General data

A total of 2980 eyes of 1490 participants with AC from the HES cohort were eligible for inclusion in this study. A total of 147 eyes were excluded from the analyses: 27 eyes with open angles, 13 eyes without gonioscopy results, 11 eyes with anterior segment abnormalities, 39 eyes with no or poor-quality AS-OCT images, and 57 eyes with ELV as the major AC mechanism. A total of 11,332 AS-OCT images of 1455 participants (2833 eyes) with AC were included. A total of 297 AS-OCT images were excluded because of poor image quality. Thus, the final dataset comprised 11,035 AS-OCT images of 1455 participants (2833 eyes) with AC (Fig. 1).

The mean age of the participants was 61.5 ± 9.2 years. A total of 474 (32.6 %) participants were males, and 981 (67.4 %) participants were females. Among the 2833 included eyes, 1672 had PACS, 182 had PAC, and 979 had AC on the AS-OCT images.

Based on the ground truth labels, 177 eyes (6.3 %) had a single AC mechanism detectable on the AS-OCT images (PB, 135 eyes; PIC, 42 eyes; TPIR, 0 eyes). A total of 2656 eyes (93.7 %) had multiple AC mechanisms detectable on the AS-OCT images (PB + PIC, 289 eyes; PB + TPIR, 647 eyes; PIC + TPIR, 168 eyes; and PB + PIC + TPIR, 1552 eyes) (Supplementary Fig. 2). The characteristics of the enrolled participants and their eyes are presented in Table 1.

3.3. Cross-validation

The 11,035 AS-OCT images were randomly divided into five independent datasets, each comprising 2207 images, with four datasets for cross-validation and one dataset for the held-out test (Table 2 and Supplementary Table 1). An overview of the performance of the model (confusion matrices and ROC curves) for the four-fold cross-validation is presented in Fig. 2(A–I).

Our models (CMD-Net, represented by the blue lines) achieved excellent performance in classifying AC mechanisms and outperformed the baseline models (represented by the orange lines) with a mean AUC of 0.980 (95 % CI, 0.975–0.985) compared to 0.969 (95 % CI, 0.963–0.976) in the validation sets. The best-performing model was selected as the final prediction model. This model (CMD-Net on fold-3) achieved an AUC of 0.981 (95 % CI, 0.976–0.986), an accuracy of 90.3 % (95 % CI, 89.0%–91.5 %), a sensitivity of 89.3 % (95 % CI, 86.7%–91.3 %), and a specificity of 94.7 % (95 % CI, 93.5%–95.8 %).

3.4. Human-machine comparison

Human-machine comparisons were performed for the held-out and separate test sets (Table 2 and Supplementary Table 1). Predictions from the model and three glaucoma specialists were obtained for each image. Fig. 3 (A–E) and Fig. 4 (A-E) present the

Table 1
Characteristics of the study participants/eyes.

Parameter	Participants/eyes (n = 1455/2833)
Age (Mean ± SD), years	61.5 ± 9.2
Gender	
Male (%)	474 (32.6)
Female (%)	981 (67.4)
Diagnosis	
Eyes with PACS (%)	1672 (59.0)
Eyes with PAC (%)	182 (6.4)
Eyes with 90° ≤ ITC < 180° plus angle-closure on ASOCT images (%)	979 (34.6)
Eyes with a single Angle-Closure mechanism (%)	177 (6.3 %)
Solely PB	135
Solely PIC	42
Solely TPIR	None
Eyes with multiple Angle-Closure mechanisms (%)	2656 (93.7 %)
PB + PIC	289
PB + TPIR	647
PIC + TPIR	168
PB + PIC + TPIR	1552

SD, standard deviation; PACS, suspected primary angle-closure; PAC, primary angle-closure; ITC, iridotrabecular contact; AS-OCT, anterior segment optical coherence tomography; PB, pupillary block; PIC, plateau iris configuration; TPIR, thick peripheral iris roll.

Table 2
Performance of our models and ophthalmologists in the cross-validation, held-out, and separate test sets.

Cross-validation set	AUC (95 %CI)	Accuracy (95 % CI) (%)	Sensitivity (95 % CI) (%)	Specificity (95 % CI) (%)
CMD-Net on fold 1	0.978 (0.972–0.983)	89.9 (88.6–91.1)	88.8 (86.2–91.0)	94.6 (93.4–95.7)
CMD-Net on fold 2	0.980 (0.975–0.985)	90.4 (89.1–91.6)	90.2 (87.8–92.1)	95.1 (93.9–96.1)
CMD-Net on fold 3	**0.981 (0.976–0.986)**	90.3 (89.0–91.5)	89.3 (86.7–91.3)	94.7 (93.5–95.8)
CMD-Net on fold 4	0.980 (0.975–0.986)	90.3 (89.0–91.5)	89.7 (87.2–91.7)	94.9 (93.7–95.9)
Held-out test set	**AUC (95 % CI)**	**Accuracy (95 % CI) (%)**	**Sensitivity (95 % CI) (%)**	**Specificity (95 % CI) (%)**
CMD-Net	**0.977 (0.971–0.982)**	89.9 (88.6–91.1)	88.8 (86.3–91.0)	94.6 (93.3–95.6)
Ophthalmologist 1	0.864 (0.848–0.880)	81.9 (80.2–83.5)	82.0 (78.9–84.6)	90.8 (89.2–92.2)
Ophthalmologist 2	0.888 (0.873–0.903)	85.0 (83.4–86.4)	85.2 (82.4–87.7)	92.4 (90.9–93.6)
Ophthalmologist 3	0.903 (0.889–0.917)	87.0 (85.5–88.3)	87.3 (84.6–89.5)	93.4 (92.0–94.6)
Separate test set	**AUC (95 % CI)**	**Accuracy (95 % CI) (%)**	**Sensitivity (95 % CI) (%)**	**Specificity (95 % CI) (%)**
CMD-Net	**0.988 (0.972–1.000)**	93.0 (88.9–95.6)	91.7 (82.5–96.3)	95.7 (91.3–97.7)
Ophthalmologist 1	0.843 (0.789–0.897)	80.7 (75.1–85.3)	78.8 (68.2–86.3)	89.8 (84.1–93.4)
Ophthalmologist 2	0.860 (0.810–0.910)	80.7 (75.1–85.3)	81.7 (71.4–88.3)	90.4 (85.0–93.7)
Ophthalmologist 3	0.891 (0.843–0.938)	86.8 (81.8–90.6)	85.1 (75.1–91.4)	93.0 (87.8–96.0)

AUC, area under the receiver operating characteristic curve; CI, confidence interval.

performances of the specialists and the model in the held-out and separate test sets, respectively.

The performance of CMD-Net exceeded the performance of all three human experts in classifying AC mechanisms. On the held-out test set (2207 AS-OCT images), CMD-Net achieved an AUC of 0.977 (95 % CI, 0.971–0.982), an accuracy of 89.9 % (95 % CI, 88.6%–91.1 %), a sensitivity of 88.8 % (95 % CI, 86.3%–91.0 %), and a specificity of 94.6 % (95 % CI, 93.3%–95.6 %). The average performance of the three ophthalmologists had an AUC of 0.885 (95 % CI, 0.870–0.900) and an accuracy of 84.6 % (95 % CI, 83.0%–86.1 %). The best-performing ophthalmologist achieved an AUC of 0.903 (95 % CI, 0.889–0.917), an accuracy of 87.0 % (95 % CI, 85.5%–88.3 %), a sensitivity of 87.3 % (95 % CI, 84.6%–89.5 %), and a specificity of 93.4 % (95 % CI, 92.0%–94.6 %).

CMD-Net showed good generalizability in the separate test set (228 AS-OCT images). The model outperformed all human experts, with an AUC of 0.988 (95 % CI, 0.972–1.000), an accuracy of 93.0 % (95 % CI, 88.9%–95.6 %), a sensitivity of 91.7 % (95 % CI, 82.5%–96.3 %), and a specificity of 95.7 % (95 % CI, 91.3%–97.7 %). The best-performing ophthalmologist achieved an AUC of 0.891 (95 % CI, 0.843–0.938), an accuracy of 86.8 % (95 % CI 81.8%–90.6 %), a sensitivity of 85.1 % (95 % CI, 75.1%–91.4 %), and a specificity of 93.0 % (95 % CI, 87.8%–96.0 %).

These results mean that the AI model was able to classify AC types more accurately than highly trained glaucoma specialists.

3.5. *Interpretation*

The heat maps created in this study (Fig. 5) show clinically relevant eye structures that CMD-Net focused on when making final decisions. For PB (Fig. 5A), CMD-Net typically focused on the iris, lens, and the central and peripheral anterior chamber, as indicated by the rectangles in Fig. 5G. For PIC (Fig. 5B), CMD-Net tended to focus on the entire iris as well as the angles (Fig. 5H), whereas for TPIR (Fig. 5C), the focus was largely on the folded part of the iris (Fig. 5I). Conversely, Inception-V4 showed no specific tissue foci of attention (Fig. 5D–F). This suggests CMD-Net learned to examine images similarly to how human experts would, focusing on the key anatomical features that distinguish different AC mechanisms.

4. Discussion

This study presents a novel deep learning model, CMD-Net, for automated classification of AC mechanisms from AS-OCT images [26]. By leveraging a hierarchical vision transformer architecture and distilling strategy, CMD-Net outperformed traditional diagnostic methods, including human expert evaluation, achieving higher accuracy, sensitivity, and specificity. And the performance of the model was superior to that of the baseline model without a distilling strategy. Good interpretability was shown compared with that of the state-of-the-art CNN model, Inception-V4. In addition, this study also demonstrated the generalizability of CMD-Net on some level. Thus, the findings of the present study highlight the potential of our innovative approach to improve diagnostic accuracy and standardization in the assessment of AC mechanisms. However, we acknowledge that further external validation on diverse datasets is needed to establish the generalizability of our findings. Hence, we propose conducting multi-center studies across various geographic regions and ethnic groups to assess the model's performance and adaptability in diverse populations. Additionally, we plan to evaluate the model's performance across different clinical settings and conduct longitudinal studies to assess its predictive value over time.

The accurate identification of AC mechanisms plays a crucial role in clinical practice. In patients with PACS and narrow angles, AC can be eliminated by favorably altering anterior segment configuration to prevent PAS formation and IOP elevation [36]. Prophylactic interventions for PB include the administration of topical miotics and LPI [9,12–14,37]. ALPI is usually effective in inducing iris stromal contraction to pull the iris root away from the angle wall and reducing peripheral iris crowding in patients with PIC or TPIR who may experience recurrent IOP elevation associated with creeping AC following LPI [7,9,10,15,37,38]. Lens extraction is the treatment of choice in cases where ELV is the dominant AC mechanism as it often provides definitive treatment and prevents GON [6,7,

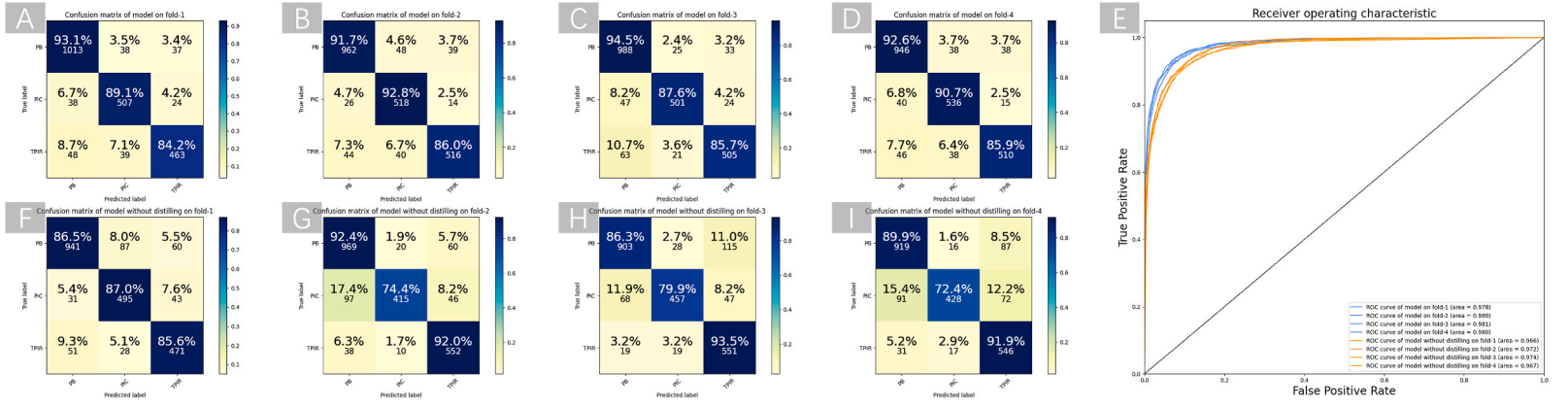

Fig. 2. Model performance in the cross-validation set. A–D and F–I show the confusion matrices of our model and the baseline model, respectively. E shows the receiver operating characteristic curves with the blue lines representing our model and orange lines representing the baseline model.

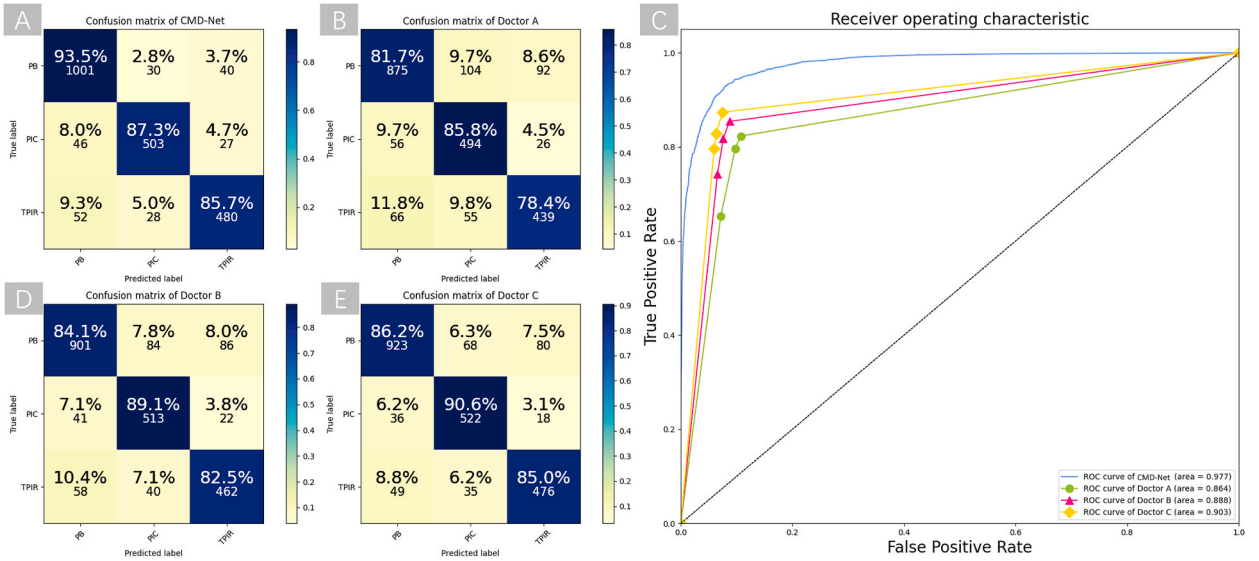

Fig. 3. Human-machine comparison in the held-out test set. Confusion matrices of our model and those of the three ophthalmologists are shown in A, B, D, and E. The receiver operating characteristic curves are shown in C.

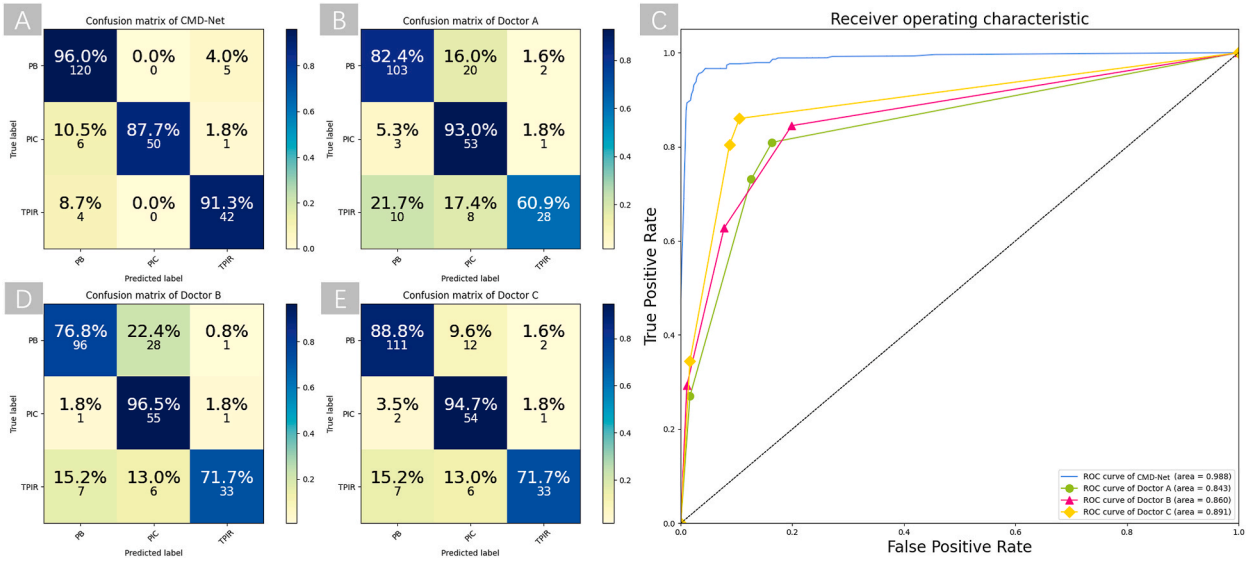

Fig. 4. Human-machine comparison in the separate test set. The confusion matrices of our model and those of the three ophthalmologists are shown in A, B, D, and E. The receiver operating characteristic curves are shown in C.

16,37]. Several interventions may be indicated for the same eye in the presence of multiple AC mechanisms. Therefore, it is prudent to note that the use of automated methods to identify AC mechanisms does not obviate the requirement to sequentially re-evaluate anterior segment configuration following any intervention.

Previous studies have shown that the majority of patients with PACD in China have multiple, simultaneous mechanisms contributing to AC in the same eye, which is in contrast to Caucasian patients with PACD, in whom PB is the most common causative mechanism [9,11,15]. Wang et al. reported the following breakdown of AC mechanisms in the eyes of Chinese patients based on UBM images: pure PB (38.1 %), pure non-PB (7.1 %, subtypes: anteriorly positioned ciliary body and iris crowding), and multiple mechanisms (54.8 %, subtypes: PB and coexistent iris crowding; PB and coexistent anterior ciliary body positioning or all three mechanisms simultaneously) [11].

And this study confirms the expected multifactorial nature of AC in this population. Only 177 eyes (6.25 %) had a single-acting AC mechanism, whereas the remainder had multiple coexisting AC mechanisms. This proportion is significantly lower than the proportion of eyes with a single-acting AC mechanism reported by Wang et al. [10] This may be attributed to the disparate study populations, with

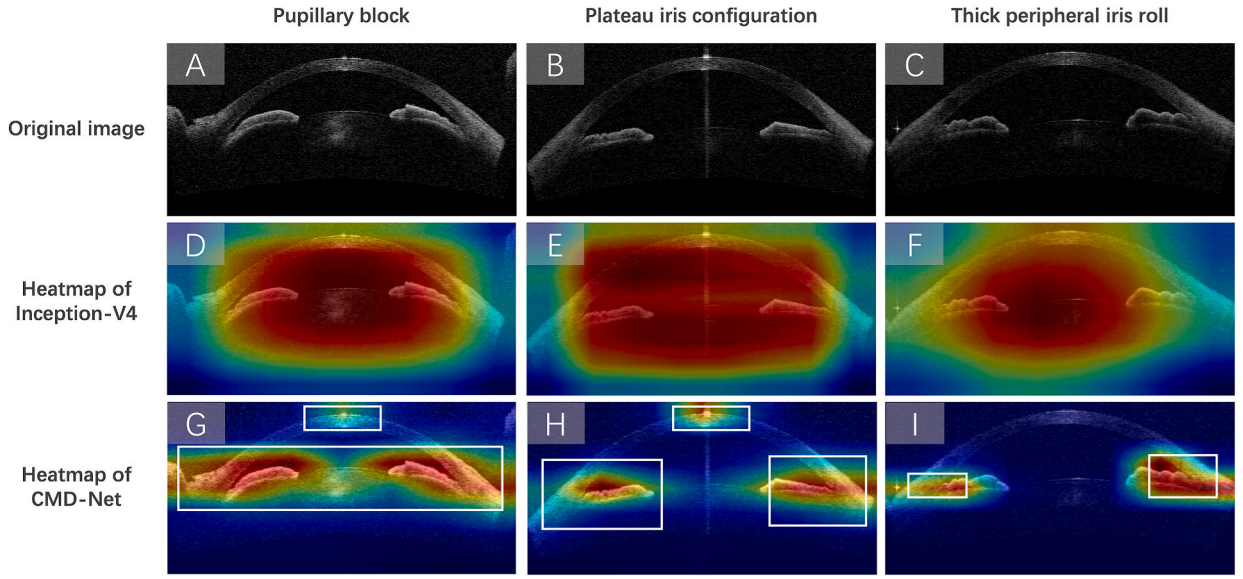

Fig. 5. Heatmaps for model attention for three typical angle-closure mechanisms. Original AS-OCT images are shown with the corresponding heatmaps for Inception-V4 and CMD-Net for pupillary block (A, D, G), plateau iris configuration (B, E, H), and thick peripheral iris roll (C, F, I). AS-OCT: anterior segment optical coherence tomography.

predominantly PACS included in our study compared with the previous study, which predominantly included patients with AACC and PACG [11]. Moreover, the methodology followed in our study varied significantly, as it utilized four-quadrant AS-OCT images per eye, unlike single cross-sectional UBM images, which were used in the study by Wang et al. [11] It was also observed that AS-OCT images in some individuals displayed distinct AC mechanisms 180° apart within the same eye (Fig. 6 [A, B]), which highlights the potential of single-image analysis to result in misclassification.

Several other studies have used UBM imaging. UBM imaging is a contact method that requires topical anesthesia and a water bath, with the attendant risks of infection and corneal abrasion, that is demanding in terms of time and requisite operator skill [7,18]. Angle configuration may be affected by the inadvertent application of pressure on the globe and the posterior displacement of the iris-lens diaphragm induced by a supine position [18]. Moreover, it is not possible to determine the precise location of the angle being imaged with UBM [18]. These limitations have led to UBM being superseded by alternative techniques, such as AS-OCT.

Although the AS-OCT classification of AC mechanisms is well established; it is limited by subjectivity and the risk of misdiagnosis arising from the analysis of single cross-sectional images [10,20,21]. Analyzing images from all four quadrants of each eye may improve diagnostic accuracy at the expense of time efficiency, but this may be too time-consuming to be practical. This study establishes a deep learning algorithm that enables the accurate and automated detection of AC mechanisms that circumvents the limitations of existing methods.

Recent studies have reported advances in the application of AI in the identification of glaucoma and structural changes associated with disease progression, with important implications for the utility of AI in glaucoma care [25,39]. However, studies applying machine learning to the recognition of AC mechanisms are limited.

Wirawan et al. used an Adaboost classifier to determine AC mechanisms in 156 patients with PAC and PACG and achieved good model performance with a weighted average accuracy, sensitivity, and specificity of 84.4 %, 64.7 %, and 90.0 %, respectively [40]. Niwas et al. also used an Adaboost classifier in a sample of 122 patients with PACG and achieved an accuracy of 74.5 % using 23

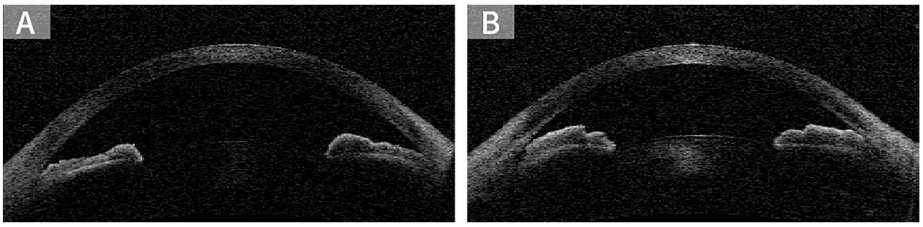

Fig. 6. AS-OCT images demonstrating distinct angle-closure mechanisms 180° apart within the same eye. (A) Plateau iris configuration affecting the left anterior chamber angle and pupillary block affecting the right anterior chamber angle, (B) pupillary block + thick peripheral iris roll affecting the left anterior chamber angle (pupillary block being the major mechanism) and plateau iris configuration + thick peripheral iris roll affecting the right anterior chamber angle (plateau iris configuration being the major mechanism). AS-OCT: anterior segment optical coherence tomography.

selected features from AS-OCT images [41]. This group conducted further studies to create an expert automated system for classifying AC mechanisms. Using AS-OCT images from 74 patients with PACG, they achieved an overall accuracy of 89.2 % with leave-one-out cross-validation and an accuracy of 85.1 % with 10-fold cross-validation [12]. However, these studies are limited by their sample sizes and case selection within clinics as opposed to the general population, which may underrepresent or exclude the early stages of the disease.

This study collated a large sample of mechanism-labeled AS-OCT images, enabling the first deep learning-based exploration of AC mechanism classification. AC mechanism classification lends itself to comprehensive judgment using a tradeoff of long-range feature relationships over whole images, necessitating an efficient architecture with a greater focus on multirange dependencies than individual features. However, this is beyond the scope of conventional CNNs. In contrast, transformer leverages the architecture to support the capture of long-range relationships via self-attention. Its efficacy has been demonstrated in image analysis and neurolinguistic programming for electronic health records [42,43]. Since AC mechanisms co-existed in most of the cases included in the present study, a teacher-student strategy was adopted to counteract the label noise. The strategy used in this study, known as "distilling," is effective in combination with a vision transformer, with the "student" outperforming the "teacher" as measured by the tradeoff between accuracy and throughput [30,44]. The deep learning network developed in the present study outperformed the same classification network without a distilling strategy, especially in the identification of TPIR. The model also outperformed the experts, indicating its potential to be a useful and standard adjunct to clinical decision-making in supporting the optimal care of patients with PACD and its ability of reducing variability and potentially catching cases that may be missed by human evaluation alone.

This study was population-based; therefore, the observed results may be more generalizable than those of studies using participants recruited from clinics. Cases of PACS and cases with anatomically narrow drainage angles outweighed cases of PAC and PACG in the cohort of the present study. It is arguably of greater value to accurately distinguish AC mechanisms to guide treatment in the early stages of PACD, as surgery is often the default treatment for late-stage disease [37].

Nevertheless, the present study has some limitations. First, we excluded images with ELV as the main AC mechanism. Our population-based sample comprised relatively few cases of PACG, where ELV mechanisms tend to feature more prominently [8]. We aim to enroll more patients with PACG from clinics to increase the number of AS-OCT images with ELV as the dominant AC mechanism in future studies. Second, the relative contribution of an anteriorly positioned ciliary body from that of an anteriorly inserted iris in eyes with PIC could not be distinguished as visualization of the ciliary body using AS-OCT is limited. However, we believe that these subtle distinctions may not hinder the clinical utility of the model as the optimal treatment options for each anatomical scenario remained unchanged. Third, all our participants were rural Northern Chinese. While our rural-based sample may better represent the broader Chinese population compared to urban cohorts, we acknowledge that this could limit generalizability to other ethnicities or regions. Future studies evaluating the model in diverse populations are needed. Fourth, the cross-validation and held-out test sets were split at the image level rather than by patient, which could potentially inflate performance estimates if multiple images from the same patient ended up in both sets. Further validation studies should be performed on patient-level. Finally, there was an important limitation regarding the significant computational resources needed for training the Swin-Transformer on a large-scale glaucoma OCTA dataset, this might not be feasible for all research settings, particularly those with limited access to advanced computational infrastructure. However, the computational demands significantly decrease once the model is trained. During the deployment phase, the model can operate efficiently on more modest computational systems, which is beneficial for clinical applications and smaller research settings. In our future work, potential strategies will mitigate these challenges, such as transfer learning and model compression, which can help adapt the use of these models in resource-constrained environments.

5. Conclusions

This study developed automated deep learning algorithms for classifying AC mechanisms that outperform existing manual and subjective methods, which might assist clinicians in making appropriate treatment decisions and can also be applied to explore the risk factors associated with the development of PACD in eyes with varying AC mechanisms. And prospective clinical validation studies and longitudinal follow-up are further needed to assess real-world performance and utility of the model as a decision support tool.

Funding

This study was supported by the Beijing Hospitals Authority Youth Program (Grant Number QML20210201) and the Research Special Fund of the Ministry of Health of the People's Republic of China (Grant Number 201002019). The funding organizations had no role in the design or conduct of the study.

Data Sharing Statement: The authors declare that all data supporting he findings of this study are available within the paper. They are not publicly available, and restrictions apply to their use. All requests would require evaluation on an individual basis and can be made by contacting wningli@vip.163.com.

CRediT authorship contribution statement

Ye Zhang: Writing – original draft, Project administration, Methodology, Investigation, Funding acquisition, Formal analysis, Conceptualization. **Xiaoyue Zhang:** Writing – original draft, Project administration, Methodology, Investigation, Data curation, Conceptualization. **Qing Zhang:** Validation, Project administration, Data curation. **Bin Lv:** Resources, Data curation. **Man Hu:** Writing – review & editing, Validation. **Chuanfeng Lv:** Validation, Resources. **Yuan Ni:** Resources. **Guotong Xie:** Writing – review & editing,

Validation, Resources. **Shuning Li:** Writing – review & editing, Validation, Resources, Conceptualization. **Nazlee Zebardast:** Writing – review & editing, Validation. **Yusrah Shweikh:** Writing – review & editing, Validation. **Ningli Wang:** Writing – review & editing, Validation, Supervision, Resources, Project administration, Funding acquisition, Conceptualization.

Declaration of competing interest

The authors declare that they have no known competing financial interests or personal relationships that could have appeared to influence the work reported in this paper.

Acknowledgements

Ethics Statement: The study was approved by the Ethics Committee of the Beijing Tongren Hospital (Approval No. TREC2006-22), and written informed consent was obtained from all the participants.

Appendix A. Supplementary data

Supplementary data to this article can be found online at https://doi.org/10.1016/j.heliyon.2024.e35236.

References

[1] H.A. Quigley, A.T. Broman, The number of people with glaucoma worldwide in 2010 and 2020, Br. J. Ophthalmol. 90 (2006) 262–267.
[2] Y.C. Tham, X. Li, T.Y. Wong, et al., Global prevalence of glaucoma and projections of glaucoma burden through 2040: a systematic review and meta-analysis, Ophthalmology 121 (2014) 2081–2090.
[3] P.J. Foster, G.J. Johnson, Glaucoma in China: how big is the problem? Br. J. Ophthalmol. 85 (2001) 1277–1282.
[4] P.J. Foster, R. Buhrmann, H.A. Quigley, et al., The definition and classification of glaucoma in prevalence surveys, Br. J. Ophthalmol. 86 (2002) 238–242.
[5] N.L. Wang, W.B. Zhou, T.C. Ye, et al., Clinical researches of primary angle closure glaucoma, Chin. J. Ophthalmol. 31 (1995) 133–136.
[6] C. Wright, M.A. Tawfik, M. Waisbourd, et al., Primary angle-closure glaucoma: an update, Acta Ophthalmol. 94 (2016) 217–225.
[7] S.J. Gedde, P.P. Chen, K.W. Muir, et al., Primary angle-closure disease preferred practice pattern, Ophthalmology 128 (2021) P30–P70.
[8] S. Moghimi, R. Chen, N. Hamzeh, et al., Qualitative evaluation of anterior segment in angle closure disease using anterior segment optical coherence tomography, J Curr Ophthalmol 28 (2016) 170–175.
[9] N.L. Wang, H.P. Wu, Z.G. Fan, Primary angle closure glaucoma in Chinese and Western populations, Chin. Med. J. 115 (2002) 1706–1715.
[10] P. Tarongoy, C.L. Ho, D.S. Walton, Angle-closure glaucoma: the role of the lens in the pathogenesis, prevention, and treatment, Surv. Ophthalmol. 54 (2009) 211–225.
[11] N. Wang, J. Ouyang, W. Zhou, et al., Multiple patterns of angle closure mechanisms in primary angle closure glaucoma in Chinese, Zhonghua Yan Ke Za Zhi 36 (2000) 46–51, 5, 6.
[12] S.I. Niwas, W. Lin, X. Bai, et al., Automated anterior segment OCT image analysis for Angle Closure Glaucoma mechanisms classification, Comput. Methods Progr. Biomed. 130 (2016) 65–75.
[13] C.K. Leung, W.M. Chan, C.Y. Ko, et al., Visualization of anterior chamber angle dynamics using optical coherence tomography, Ophthalmology 112 (2005) 980–984.
[14] M. He, D.S. Friedman, J. Ge, et al., Laser peripheral iridotomy in eyes with narrow drainage angles: ultrasound biomicroscopy outcomes. The Liwan Eye Study, Ophthalmology 114 (2007) 1513–1519.
[15] M. He, P.J. Foster, G.J. Johnson, et al., Angle-closure glaucoma in East Asian and European people. Different diseases? Eye 20 (2006) 3–12.
[16] A. Azuara-Blanco, J. Burr, C. Ramsay, et al., Effectiveness of early lens extraction for the treatment of primary angle-closure glaucoma (EAGLE): a randomised controlled trial, Lancet 388 (2016) 1389–1397.
[17] M. Matsuo, S. Mizoue, K. Nitta, et al., Intraobserver and interobserver agreement among anterior chamber angle evaluations using automated 360-degree gonio-photos, PLoS One 16 (2021) e0251249.
[18] T. Dada, R. Sihota, R. Gadia, et al., Comparison of anterior segment optical coherence tomography and ultrasound biomicroscopy for assessment of the anterior segment, J. Cataract Refract. Surg. 33 (2007) 837–840.
[19] N. Porporato, M. Baskaran, R. Husain, et al., Recent advances in anterior chamber angle imaging, Eye 34 (2020) 51–59.
[20] N. Shabana, M.C. Aquino, J. See, et al., Quantitative evaluation of anterior chamber parameters using anterior segment optical coherence tomography in primary angle closure mechanisms, Clin. Exp. Ophthalmol. 40 (2012) 792–801.
[21] Y. Zhang, S.Z. Li, L. Li, et al., Quantitative analysis of iris changes following mydriasis in subjects with different mechanisms of angle closure, Invest. Ophthalmol. Vis. Sci. 56 (2015) 563–570.
[22] Y. Zhang, X. Tang, N.L. Wang, The reproducibility of mechanism categories of angle closure using ultrasound biomicroscopy and anterior segment optical coherence tomograph, Chinese J. Exp. Ophthalmol. 34 (2016) 936–940.
[23] E.L. Mayro, M. Wang, T. Elze, et al., The impact of artificial intelligence in the diagnosis and management of glaucoma, Eye 34 (2020) 1–11.
[24] J.O. Li, H. Liu, D.S.J. Ting, et al., Digital technology, tele-medicine and artificial intelligence in ophthalmology: a global perspective, Prog. Retin. Eye Res. 82 (2021) 100900.
[25] C.G. Campbell, D.S.W. Ting, P.A. Keane, et al., The potential application of artificial intelligence for diagnosis and management of glaucoma in adults, Br. Med. Bull. 134 (2020) 21–33.
[26] Z. Liu, Y.T. Lin, Y. Cao, et al., Swin Transformer: Hierarchical Vision Transformer Using Shifted Windows, 2021 14030 arXiv preprint arXiv:2103.
[27] Y.B. Liang, D.S. Friedman, T.Y. Wong, et al., Rationale, design, methodology, and baseline data of a population-based study in rural China: the Handan Eye Study, Ophthalmic Epidemiol. 16 (2009) 115–127.
[28] Y. Zhang, S.Z. Li, L. Li, et al., Quantitative analysis of iris changes after physiologic and pharmacologic mydriasis in a rural Chinese population, Invest. Ophthalmol. Vis. Sci. 55 (2014) 4405–4412.
[29] Y. Zhang, S.Z. Li, L. Li, et al., The Handan Eye Study: comparison of screening methods for primary angle closure suspects in a rural Chinese population, Ophthalmic Epidemiol. 21 (2014) 268–275.
[30] G. Hinton, V. Oriol, D. Jeff, Distilling the Knowledge in a Neural Network, 2015 02531 arXiv preprint arXiv:1503.
[31] C. Szegedy, S. Ioffe, V. Vanhoucke, et al., Inception-v4, inception-resnet and the impact of residual connections on learning, in: Thirty-First AAAI Conference on Artificial Intelligence, 2017.

[32] J. Deng, W. Dong, R. Socher, et al., ImageNet: a large-scale hierarchical image database, in: 2009 IEEE Conference on Computer Vision and Pattern Recognition, 2009.
[33] T. Fawcett, An introduction to ROC analysis, Pattern Recogn. Lett. 27 (2006) 861–874.
[34] M.S. Wandishin, S.J. Mullen, Multiclass ROC analysis, Weather Forecast. 24 (2009) 530–547.
[35] R.R. Selvaraju, M. Cogswell, A. Das, et al., Grad-Cam: visual explanations from deep networks via gradient-based localization. Proceedings of the IEEE International Conference on Computer Vision, 2017, pp. 618–626.
[36] American Academy of Ophthalmology Glaucoma Panel, Preferred Practice Pattern Guidelines: Primary Angle Closure, American Academy of Ophthalmology, San Francisco, CA, 2010.
[37] X.H. Sun, Y. Dai, Y. Chen, et al., Primary angle closure glaucoma: what we know and what we don't know, Prog. Retin. Eye Res. 57 (2017) 26–45.
[38] D.L. Junqueira, V.G. Prado, F.S. Lopes, et al., Non-pupillary block angle-closure mechanisms: a comprehensive analysis of their prevalence and treatment outcomes, Arq. Bras. Oftalmol. 77 (2014) 360–363.
[39] H.B. Dick, T. Schultz, R.D. Gerste, Miniaturization in glaucoma monitoring and treatment: a review of new technologies that require a minimal surgical approach, Ophthalmol Ther 8 (2019) 19–30.
[40] A. Wirawan, C.K. Kwoh, P.T.K. Chew, et al., Feature selection for computer-aided angle closure glaucoma mechanism detection, J. Med. Imaging Health Inform. 2 (2012) 438–444.
[41] S.I. Niwas, W. Lin, X. Bai, et al., Reliable feature selection technique for automated angle closure glaucoma mechanism detection, J. Med. Syst. 39 (2015) 21.
[42] J.A. Fries, E. Steinberg, S. Khattar, et al., Ontology-driven weak supervision for clinical entity classification in electronic health records, Nat. Commun. 12 (2021) 2017.
[43] S. Yu, K. Ma, Q. Bi, et al., MIL-VT: multiple instance learning enhanced vision transformer for fundus image classification, in: Medical Image Computing and Computer Assisted Intervention – MICCAI 2021, Springer, Cham, 2021 12908.
[44] H. Touvron, M. Cord, M. Douze, et al., Training data-efficient image transformers & distillation through attention. International Conference on Machine Learning, 2021 12877 arXiv:2012.